Planar Common-Mode EMI Filter Design and Optimization for High-Altitude 100 kW SiC Inverter/Rectifier System

Xingchen Zhao, *Student Member, IEEE,* Jiewen Hu, *Student Member, IEEE*, Lakshmi Ravi, *Student Member, IEEE*, Dong Dong, *Senior Member, IEEE*, Rolando Burgos, *Senior Member, IEEE,* Sriram Chandrasekaran, and Richard Eddins

Abstract **- Silicon-Carbide (SiC) devices are receiving popularity for high-power converter systems in aircrafts due to many advantages over silicon counterparts. However, the electro-magnetic interference (EMI) problems are more serious with the SiC devices operating at higher switching speed and higher switching frequency. The common-mode (CM) EMI filter design of the high-power SiC converter is especially challenging for high-altitude application due to the harsher requirements of insulation and heat dissipation. The optimization of the parameters and physical design of a CM EMI filter in a 100-kW SiC inverter/rectifier system operating at 50,000 ft is conducted in this paper to obtain the highest power density. The effect of the switching frequency on the EMI filter volume and the total power density of the converter system is analyzed. The lower breakdown voltage of air and higher thermal resistance of natural convection make the conventional design of the CM choke infeasible at high altitudes. A PCB-based planar CM choke is designed with the consideration of partial discharge (PD) and heat dissipation at the altitude of 50,000 ft. The structure of the CM choke is optimized with embedded electric-field shielding plates, which controls electric-field intensity in the air below 300 V/mm. The PCB windings improve the efficiency of heat dissipation at high altitudes and reduce the profile of the CM choke. A Pareto optimization is conducted to minimize the size of the choke and the volume of the final design is only 155 cm^3. The experimental results show that the CM noise is reduced effectively with the CM EMI filter. PD is not observed even at the altitude of 50,000 ft and the thermal performance is excellent with a current of 190 A. With the optimization and the dedicated design of the CM EMI filter, the power density of the converter system is up to 33.3 kW/L.**

Index Terms **– EMI filter, Silicon-Carbide, Inverter, Rectifier, High altitude, Partial discharge, Heat dissipation.**

I. Introduction

Hybrid and full electric propulsion and all-electric aircrafts are more and more attractive due to its lower weight, cost, emission, and higher efficiency [1-3]. The high-power Silicon-Carbide (SiC) converter plays an important role in the more-electric aircraft due to the higher power density and lower power loss compared to the conventional Silicon-based converters [4-6]. However, the higher switching speed and higher switching frequency of SiC converters may bring higher EMI noise and the design of the EMI filter is more crucial [7-9].

With the application of SiC devices, the switching frequencies of high-power three-phase generator-rectifier and motor drive systems have been extended to nearly 100 kHz. The effect of the switching frequency on the CM EMI filter in the three-phase rectifier or inverter system should be investigated to optimize the performance of the CM EMI filter and the overall system. The required ac-side CM chokes in a SiC motor drive system with the switching frequency of 20 kHz and 200 kHz are compared based on the standard DO-160 and it is proved that a larger CM choke is needed for the case of 200 kHz [9]. [10] talks about the CM current noise under the switching frequency of 20 and 50 kHz and found that the CM current noise is higher under the switching frequency of 50 kHz. However, [9] and [10] only explores the CM EMI filter and CM current noise at two different frequencies in low-power inverters, and the numerical relationship between the switching frequency and the required CM inductance is still unclear. This relationship is highly dependent on the frequency range, EMI standard, and noise test points in the converter system. The effect of the switching frequency on the dc-side CM EMI noise and the required dc CM filter based on MIL-STD-461 CE102 in high-power three-phase inverter/rectifier system is investigated in this paper.

Compared with other applications, more efforts are required to address three additional challenges of the EMI filter design for high-altitude aviation applications: First, the low air pressure increases the thermal resistance of natural convection between windings and air [11-12]. The altitude correction factors for natural convection are given in [13] and [14] but they cannot be applied to all geometries. The effects of altitude on the thermal performance of low-voltage switch gears and control gears are investigated in [15] and the experimental results show that different components have different temperature rises at different altitudes. [16] gives the conclusion that when only pressure changes are considered, the thermal resistance of natural convection increases exponentially with increasing altitudes. The correction factors for forced air-cooling at high altitudes are explored in [17]. The effects of altitudes on the heat transfer coefficient, Nusselt number, Reynold number, and pressure loss efficient in a forced air-cooling system are investigated by experiments in [18]. The influence of altitudes on the forced air-cooling system of PCBs is investigated in [19]. However, as of today, the thermal design of the magnetic components in high-power converters operating at high altitudes is still very difficult, and a simple and practical solution is desired. The combination of

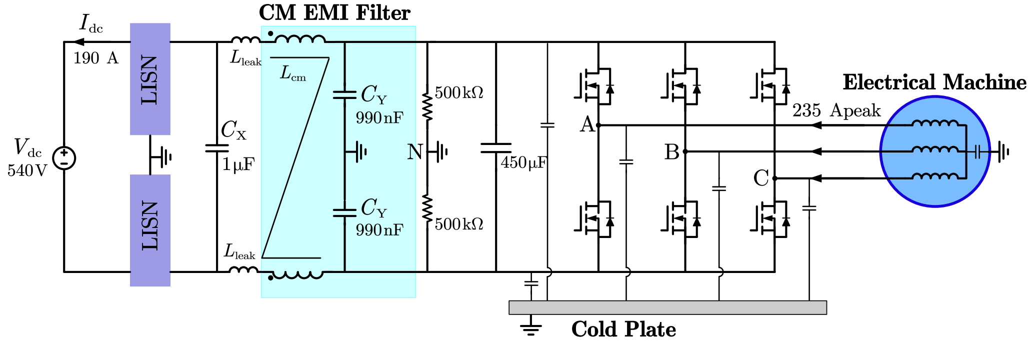

Fig. 1 The 100 kW SiC inverter/rectifier system

high current and high thermal resistance makes the heat dissipation much worse than that on the normal conditions. Potting the magnetic components and using liquid-cooling is an option, but it reduces the specific power density and introduces parasitic components to the EMI filter [20-21], so it is not considered in this project.

The second challenge for EMI filter design at high altitudes is the insulation. The low air pressure reduces the breakdown voltage of air and increases the risk of partial discharge (PD) between windings and magnetic cores. According to the Paschen's curve [22], the dielectric strength is as low as 370 V/mm at the altitude of 50,000 ft, which is much lower than the dielectric strength at the sea level (3000 V/mm). The relationship between the breakdown voltage and air pressure has been investigated for different applications such as busbar [23], gate driver [24] and electric machine [25-26]. The common finding is that the breakdown voltage decreases as the altitude increases, but for different components and geometries, the relationship between these two variables is different. The insulation of magnetic components of high-power converters operating at high altitudes has not been investigated and the measures to prevent PD have not been reported. Potting the magnetic components with epoxy is always used to control the electric-field (E-field) to prevent PD in high-voltage applications [27-28]. However, the process is complicated to eliminate any air-pocket in the potting materials, and the power density and heat dissipation get worse with this approach. Finally, the small volume and low profile are always required for the aviation system, where the conventional design of the EMI filter is not feasible.

A practical and simple method to address the three challenges has not been found in the previous literatures, and the effect of high altitudes on the EMI filter has not been quantified. In this paper, a heavy-copper planar PCB-based common-mode (CM) choke is designed for a 100-kW SiC inverter/rectifier with extra considerations of the E-field and heat dissipation at the altitude of 50,000 ft. The heat dissipation of the PCB windings is more efficient than the normal cable windings, which helps achieve a smaller volume and lower profile. The clearances between PCB windings and the magnetic core are designed carefully to enhance the insulation at the high altitude, and the shielding traces are inserted into the PCB to eliminate the PD between PCB windings and the core. The dimensions of the CM choke are optimized with the constraint of heat dissipation and E-field intensity to achieve the smallest volume. The effect of altitudes on the volume of the CM EMI filter is also analyzed. The experimental results show that the CM noise is reduced effectively with the CM EMI filter. PD is eliminated even at the altitude of 50,000 ft and the thermal performance is excellent with a current of 190 A.

The outline of this paper is as follows. In Section II, the influence of the switching frequency on the CM EMI filter and the power density of the inverter/rectifier is analyzed, and the switching frequency is optimized for the highest power density of the overall system. Section III talks about the CM choke design considering the heat dissipation and insulation at high altitudes. The CM choke design is optimization for the lowest volume. The effect of high altitudes on the volume of the CM choke is discussed. In Section IV, the EMI test results are provided to verify the effectiveness of the CM EMI filter. The thermal test and PD test of the CM choke at low air pressure are conducted to show the good heat dissipation and qualified insulation of the design CM choke. Finally, Section V shows the conclusion and future work.

II. The Influence of Switching Frequency on the CM EMI Filter and System Optimization

A. The Influence of Switching Frequency on CM EMI Filter

The diagram of the inverter/rectifier system is shown in Fig. 1. The specifications of the 100-kW inverter/rectifier system are shown in Table I. The CM EMI model of the inverter/rectifier system is show in Fig. 2. It consists of four parts: electric machine, inverter/rectifier, CM EMI filter, and line impedance stabilization network (LISN). The electric machine model includes the leakage inductance L_{EM}, the stator winding resistance R_{EM}, the parasitic capacitance between the windings $C_{winding}$, and the parasitic capacitance between

TABLE I
Specifications of the Inverter/Rectifier System

Description	**Symbol**	**Value**
DC voltage	V_{dc} (V)	540
Output dc current	I_{dc} (A)	190
Electromotive force (EMF)	*EMF* (Vrms)	200
Line frequency	f_o (Hz)	380
Modulation index	*M*	1.13
Stator inductance	L_s (μH)	200
Phase current	I_{ac} (Arms)	166
EMI standard		MIL-STD-461 CE102
Efficiency	η_1	> 99 %

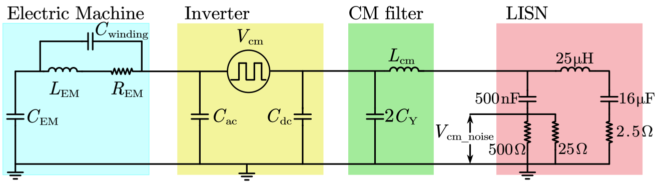

windings to the ground C_{EM} [29]. The inverter/rectifier part can be modeled as a CM voltage source, and the parasitic capacitances between the power modules and the cold plate on the dc and ac side. The parameters in the system are shown in Table II. The CM voltage source is expressed as (1).

$$V_{\mathrm{cm}} = (V_{\mathrm{AN}} + V_{\mathrm{BN}} + V_{\mathrm{CN}})/3\,. \tag{1}$$

According to MTD-STD-461 CE102, the CM EMI noise $V_{\mathrm{cm\_noise}}$ should be measured at the terminals of the 25 Ω resistor in the LISN. The CM filter consists of the 990 nF CM capacitor C_{Y} and CM choke L_{cm}. L_{cm} is designed according to the raw CM noise. The design process of L_{cm} is shown in Fig. 3. First, the Double Fourier Integral (DFI) [30] is applied to V_{cm} to obtain the spectrum of V_{cm}. $V_{\mathrm{cm\_noise}}$ at the LISN terminals can be calculated by multiplying V_{cm} with the transfer gain, then the required attenuation at different frequencies can be achieved by subtracting the limit of the EMI standard from $V_{\mathrm{cm\_noise}}$. The corner frequency f_{c} at each frequency can be calculated according to the required attenuation using the following equation.

$$f_{\mathrm{c}} = 10^{\lg(f) - \frac{A}{40}}, \tag{2}$$

where f is the frequency, and A is the required attenuation at the frequency f, which is in the logarithmic form. The lowest corner frequency is picked as the corner frequency of the CM filter, and L_{cm} can be obtained with (3).

$$L_{\mathrm{cm}} = \left(\frac{1}{2\pi f_{\mathrm{c}}}\right)^2 / (2C_{\mathrm{Y}}). \tag{3}$$

Discontinuous PWM (DPWM) for minimum loss is adopted to reduce the switching loss [31]. The spectrum of V_{cm} is obtained from DFI and is shown in Fig. 4, where the switching frequency is 70 kHz, and the slope of the envelope line is about -30 dB/dec. The transfer gain from V_{cm} to $V_{\mathrm{cm\_noise}}$ is shown in Fig. 5. There are two resonant points in the transfer gain. The first resonant frequency f_{r1} is determined by the parameters of the electric machine, as show in (4). The second resonant frequency f_{r2} is caused by the resonance between L_{EM}, C_{EM}, and C_{ac}, as shown in (5).

$$f_{r1} = \frac{1}{2\pi\sqrt{L_{\mathrm{EM}} * (C_{\mathrm{EM}} + C_{\mathrm{winding}})}}\,. \tag{4}$$

$$f_{r2} = \frac{\sqrt{\dfrac{C_{ac} + C_{\mathrm{EM}}}{L_{\mathrm{EM}} \cdot C_{ac} \cdot C_{\mathrm{EM}}}}}{2\pi}\,. \tag{5}$$

The slope of the transfer gain before f_{r1} is close to 40 dB/dec. The slope of 40 dB/dec consists of two parts: L_{EM} and C_{EM} provide the slope of 20 dB/dec, and the LISN provides the other 20 dB/dec.

TABLE II
Parameters of the CM Model

Description	Symbol	Value
Capacitor between winding and ground	C_{EM} (nF)	2.4
Leakage inductance of the electric machine	L_{EM} (μH)	14
Resistance of the stator winding	R_{EM} (Ω)	0.33
Parasitic capacitance between windings	C_{winding} (pF)	12.5
AC side parasitic capacitance	C_{ac} (nF)	0.6
DC side parasitic capacitance	C_{dc} (nF)	0.4
CM voltage source	V_{cm} (V_{peak})	270
CM inductance	L_{cm} (μH)	100.3
CM filter capacitance	C_{Y} (nF)	990

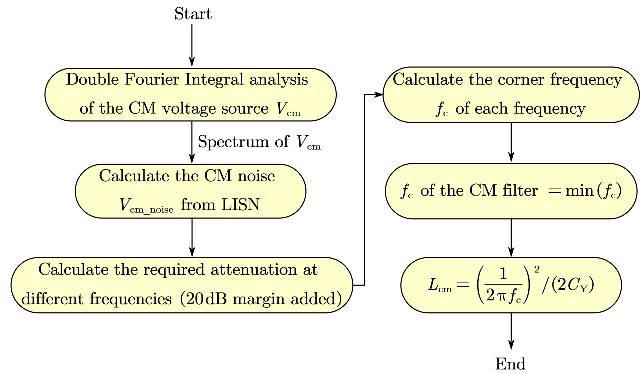

Fig. 3 The parameter design process of the CM choke

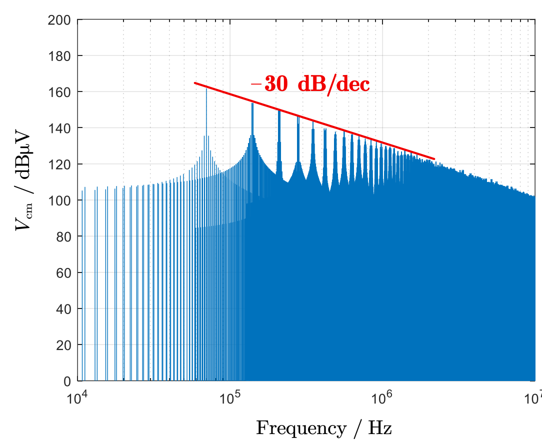

Fig. 4 The V_{cm} spectrum with f_s of 70 kHz

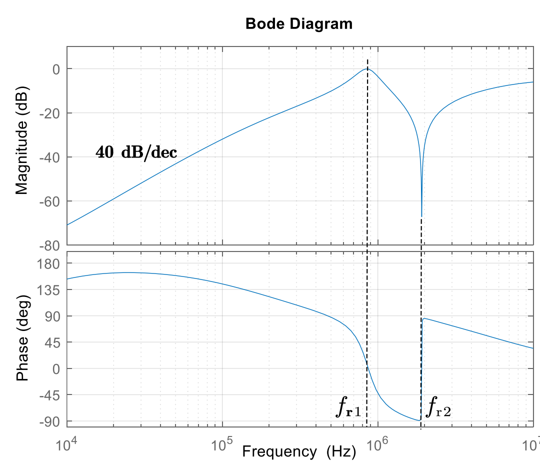

Fig. 5 The transfer gain from V_{cm} to $V_{\mathrm{cm\_noise}}$

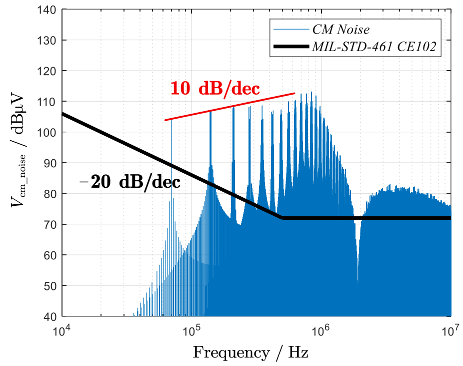

(a)

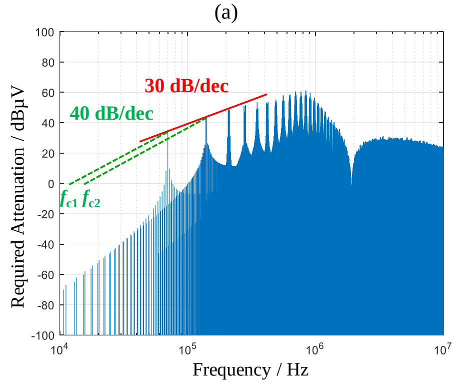

(b)

Fig. 6 The CM noise and required attenuation with f_s of 70 kHz (a) The CM noise (b) The required attenuation

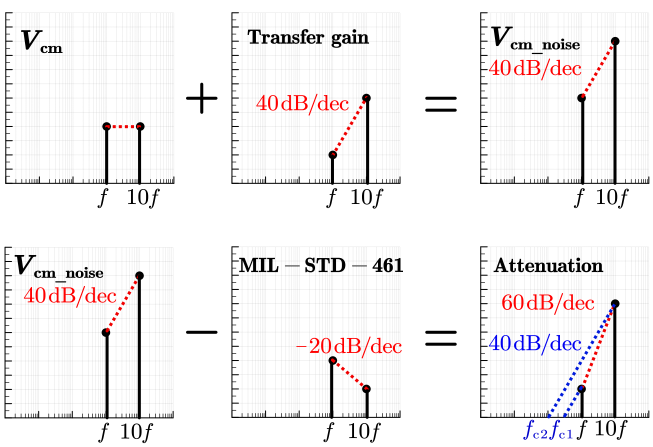

Fig. 7 The effects of switching frequency on the CM EMI filter

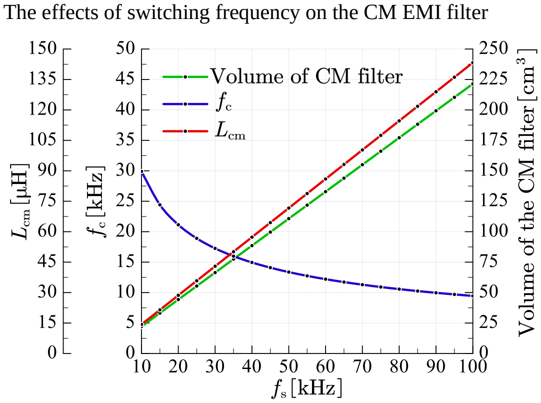

Fig. 8 The corner frequencies, required CM inductance, and the volume of the CM filter at different frequencies

The CM noise measured from LISN terminals V_{cm_noise} is the product of V_{cm} and the transfer gain from V_{cm} to V_{cm_noise} with an additional attenuation of -20 dB according to MIL-STD-461 CE102. V_{cm_noise} with the switching frequency of 70 kHz is plotted in Fig. 6(a). It can be observed that the CM noise follows a slope of about 10 dB/dec before f_{r1}, which is a result from the -30 dB/dec of V_{cm} and 40 dB/dec of the transfer gain. Based on MIL-STD-461 CE102, the required attenuation is shown in Fig. 6(b), where a margin of 20 dB is included. The first stage of the standard shows a slope of -20 dB/dec, so the envelope of the required CM attenuation has a slope of 30 dB/dec. The LC CM filter can provide an attenuation of 40 dB/dec, so the switching frequency determines the lowest corner frequency, as shown in Fig. 6(b).

The relationship between the switching frequency and the required CM inductance are investigated. As shown in Fig. 6(b), f_c and L_{cm} are determined by the switching frequency, so only the transfer gain and attenuation at the switching frequency should be considered in the analysis. Assuming the switching frequency increases from f to $10f$, the magnitude of the CM source voltage V_{cm} keeps constant, as shown in Fig. 7. The switching frequency in high-power inverter/rectifier system is usually much lower than f_{r1}, so the difference of the transfer gain between these two frequencies is about 40 dB, which leads to a difference of 40 dB in the CM noise V_{cm_noise}. Adding the -20 dB/dec slope of the EMI standard, the required CM attenuation shows a slope of 60 dB/dec, which means the magnitude of V_{cm_noise} increases by 60 dB if the switching frequency increases by one decade. Therefore, the corner frequency decreases by 0.5 decade and the required CM inductance increases by one decade, in another word, L_{cm} is proportional to the switching frequency. Fig. 8 shows the corner frequencies, required CM inductance, and the volume of the CM filter at different frequencies. It indicates that the volume of the CM EMI filter increases proportionally with the increasing switching frequency.

B. The Selection of Switching Frequency

The analysis above shows that the higher switching frequency leads to a larger CM EMI filter. However, that does not mean a low switching frequency should be used. The optimal switching frequency should be determined to obtain the lowest volume of the whole system. The switching frequency must be higher than 25 kHz to make the output current THD lower than 2%. The efficiency at different frequencies is shown in Fig. 9. The switching frequency should not exceed 70 kHz to meet the efficiency requirement of 99%. The switching frequency is swept between 25 and 70 kHz to find the optimal switching frequency for the highest power density. The volume of the inverter/rectifier consists of three parts: CM EMI filter, dc-link capacitors, and semiconductor devices (including the cold plate). The volume of power modules and the cold plate is fixed, so the influence of the switching frequency on the capacitors is investigated to obtain the optimal switching frequency. The 30 μF film capacitor B32776G8306K from TDK is used as the dc-link capacitor. Two factors affect the dc capacitance. One is the

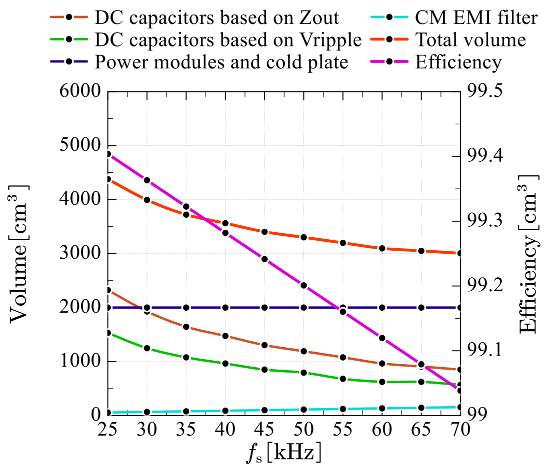

Fig. 9 The volume and efficiency with different switching frequencies

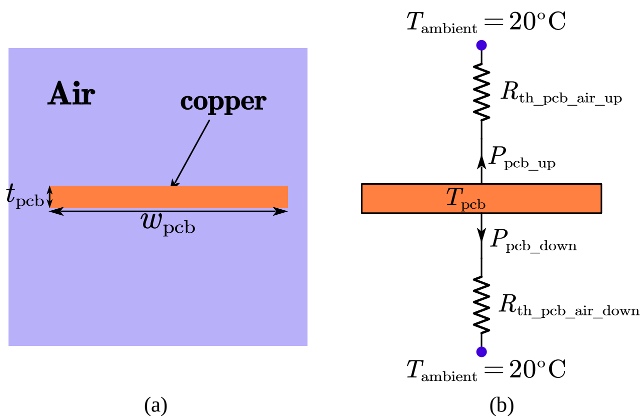

Fig. 10 The PCB winding (a) The diagram (b) The thermal model

peak output dc voltage ripple, which can be expressed as (6) [32]

$$C = 0.25 \frac{I_{\max}}{f_s V_{\text{ripple}}} , \tag{6}$$

where I_{max} is the peak phase current and V_{ripple} is the limit of the dc voltage ripple, which is 3 V in this project. Another consideration is the output impedance Z_{out} of the rectifier. Z_{out} should be lower than 0.051 Ω at the bandwidth f_{BW}, as shown in (7). The bandwidth is set to be 1/10 of f_s [33].

$$Z_{\text{out}} = \frac{1}{2\pi f_{\text{BW}} C} = \frac{10}{2\pi f_s C} < 0.051\ \Omega. \tag{7}$$

Fig. 9 shows relationship between the volume of different parts of the inverter/rectifier and the switching frequency. It shows that the volume of the capacitors is dominated by the output impedance, and the higher switching frequency leads to smaller dc capacitors. The volume of capacitors is much higher than that of the volume of CM filter, which means the power density of the converter is dominated by the dc capacitors, and higher switching frequency benefits the total power density. Finally, 70 kHz is used as the switching frequency to maximize the power density. The dc capacitance is 450 μF.

III. The CM Choke Design Considering Heat Dissipation and Insulation at High Altitudes

A. Heat Dissipation at High Altitudes

The heat dissipation is harsher at high altitudes because the lower air density leads to the higher thermal resistance of natural convection [34]. PCB winding is a good option to replace the cable to improve the thermal performance at high altitudes. The PCB winding can be modeled as a horizontal plate, as shown in Fig. 10(a). Fig. 10(b) shows the thermal model of the natural convection of the PCB winding. There are two thermal paths in the model, one is upwards to the air and the other one is downwards. The relationship between the PCB temperature T_{pcb} and the power loss of PCB P_{pcb} is shown in (8).

$$T_{\text{pcb}} - T_{\text{ambient}} = \\ (P_{\text{pcb\_up}} + P_{\text{pcb\_down}}) \cdot \left(\frac{R_{\text{th\_pcb\_air\_up}} \cdot R_{\text{th\_pcb\_air\_down}}}{R_{\text{th\_pcb\_air\_up}} + R_{\text{th\_pcb\_air\_down}}} \right), \tag{8}$$

where P_{pcb_up} and P_{pcb_down} are the power loss transferred from the top surface and bottom surface, respectively. $R_{th\_pcb\_air\_up}$ is the thermal resistance of natural convection between the top surface and the air. $R_{th\_pcb\_air\_down}$ is the thermal resistance of natural convection between the bottom surface and the air. The thermal models of the natural convection upwards and downwards are very similar, and they are introduced uniformly below. The thermal resistance between the PCB surface and air can be calculated with (9).

$$R_{\text{th\_pcb\_air}} = \frac{1}{hS} = \frac{1}{\frac{k}{L_c} Nu \cdot S}, \tag{9}$$

where h is the heat transfer coefficient. S is the surface area of the PCB. k is the thermal conductivity of the air and L_c is the characteristic length of the PCB, which is defined as (10).

$$L_c = \frac{S}{P}, \tag{10}$$

where P is the perimeter of the PCB surface area. Nu is the Nusselt number which represents the ratio between convective heat transfer and conductive heat transfer. The expression of Nu is different for the top and bottom surfaces, as shown in (11). (11) shows that the thermal resistance of the top surface is lower than that of the bottom surface.

$$Nu = \begin{cases} 0.54\,(GrPr)^{1/4}, & \text{top surface} \\ 0.27\,(GrPr)^{1/4}, & \text{bottom surface} \end{cases}, \tag{11}$$

where Gr is the Grashof number describing the relationship between the buoyance and viscosity within a fluid. Pr is the Prandtl number, which describes the relationship between momentum diffusivity and thermal diffusivity. Gr can be expressed as the following equation.

$$Gr = \frac{g {L_c}^3 \beta (T_{\text{pcb}} - T_{\text{ambient}})}{\eta^2}, \tag{12}$$

where g is the acceleration of gravity. β is the air thermal expansion coefficient. η is the kinematic viscosity of air. (12)

shows that Gr is affected by T_{pcb}, which depends on $R_{th\_pcb\_air}$ influenced by Gr in return. This means the calculation of T_{pcb} is an iterative process. The higher T_{pcb} results in a lower $R_{th\_pcb\_air}$. Pr can be expressed as (13).

$$Pr = \frac{\mu c_p}{k} = \frac{\eta \rho c_p}{k}, \tag{13}$$

where μ is the dynamic viscosity of air and is close to the product of η and the air density ρ. c_p is the air specific heat. Compared to that at sea level, $R_{th\_pcb\_air}$ at high altitudes is higher mainly due to the lower air density and the higher kinematic viscosity. T_{pcb} can be calculated with (8)-(13). The parameters used in the calculation are listed in Table III.

Based on the PCB manufacturing capability, four copper layers are embedded in the PCB and they are paralleled to share the current. The stack-up diagram of the PCB is shown in Fig. 11. For such a stack-up, the effects of FR4 on the heat dissipation and temperature difference between different copper layers should be analyzed. The total thickness of the FR4 layers is 1.4 mm, and the thermal resistance of FR4 layers can be calculated with (14).

$$R_{th\_fr4} = \frac{t_{fr4}}{kS}, \tag{14}$$

where t_{fr4} is the total thickness of FR4 layers, S is the area of the PCB, k is the thermal conductivity of FR4 material, which is 0.25 W/mK. Fig. 12 shows the thermal resistance of natural convection $R_{th\_pcb\_air}$ and R_{th_fr4} with different areas of the PCB at the altitude of 50,000 ft. Fig. 12 shows that R_{th_fr4} is much lower than $R_{th\_pcb\_air}$ and can be ignored in the thermal model.

Taking the final dimensions of the PCB winding (width 32 mm, length 158 mm) as an example, some electrical-thermal simulations are conducted with COMSOL. The dc current of 190 A flows through the PCB winding in the simulations. Fig. 13(a) shows the temperature of the cross-section area of the PCB winding with the 4-layer stack-up at the altitude of 50,000 ft, where the temperature of the third copper layer is the highest because it is the inner layer and is the far from the air on the top. The lowest temperature exists in the top copper layer as expected because the heat dissipation is more efficient on the top surface. However, the temperature difference in the whole PCB winding is within 3 °C, which proves that the FR4 layers between copper layers are not the main barrier for the heat dissipation of inner copper layers. Fig. 13(b) shows the PCB temperatures with another stack-up, where the PCB winding consists of a copper layer of 2 mm and two solder mask layers of 0.08 mm. In this configuration, the temperature of the PCB winding is almost the same as that with the 4-layer stack-up, which proves that the thermal resistance of FR4 can be ignored compared to the thermal resistance of natural convection, and the PCB winding can be modeled as a heavy-copper bar with natural convection on top and bottom sides.

The thermal model of the cable winding is similar to that of the PCB winding [30]. To compare the thermal performance of the cable and PCB winding, the temperatures of the two types of windings are calculated with the same cross-section area and length. The length of the windings is set to be 100 mm and the rated current of the winding is 190 A. The

TABLE III
Parameters in the Thermal Model

Description	Symbol	Value
Thermal conductivity of air	k	0.026 W/(m*K)
Acceleration of gravity	g	9.8 m/s^2
Thermal expansion coefficient of air	β	0.0034 K^{-1}
Kinematic viscosity of air	η	1.5e-5 m^2/s (sea level) 9.8e-5 m^2/s (50,000 ft)
Dynamic viscosity of air	μ	1.85e-5 Ns/m^2
Air density	ρ	1.23 kg/m^3 (sea level) 0.19 kg/m^3 (50,000 ft)
Air specific heat	c_p	1005 J/kg*K

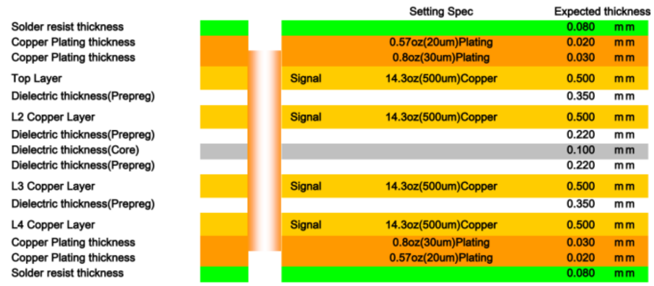

Fig. 11 The stack-up diagram of PCB

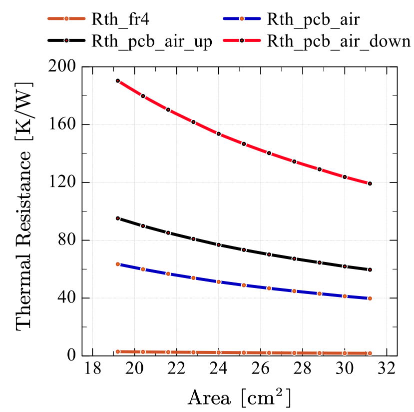

Fig. 12 $R_{th\_pcb\_air}$ and R_{th_fr4} for different dimensions of PCB

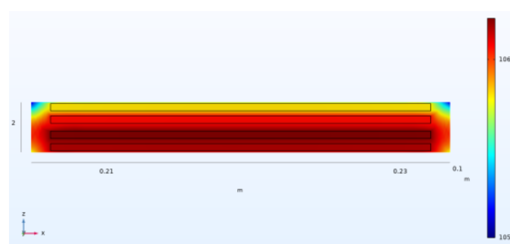
(a)

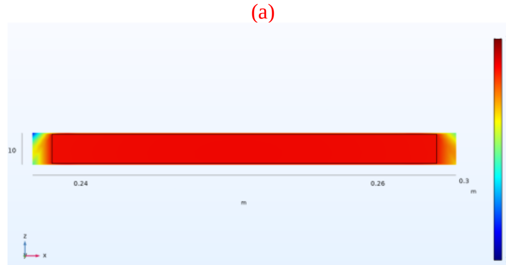
(b)

Fig. 13 Thermal simulation of two PCB stack-up (a) With the stack-up of 4 copper layers (b) With one 2-mm copper layer

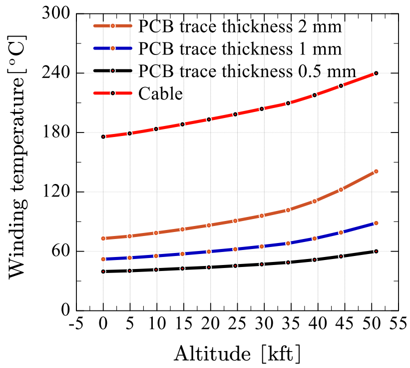

(a)

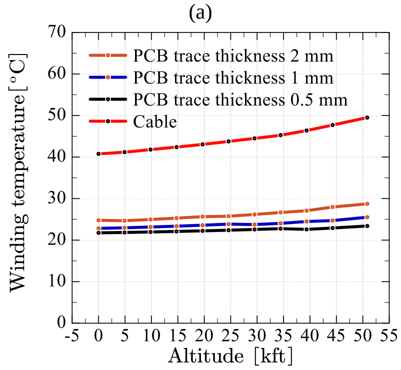

(b)

Fig. 14 The winding temperature with different types of windings and different altitudes (a) Current density 5 A/mm^2 (b) Current density 1 A/mm^2

winding temperatures with different altitudes, current densities, and winding types are show in Fig. 14. Fig. 14(a) and (b) show the winding temperatures with different current densities. Fig. 14 shows that the winding temperature increases as the altitude increases, especially with a high current density. The temperature of PCB winding is always lower than that of normal cable winding, and the difference is larger with the higher altitude and higher current density. If the thickness of the PCB trace is lower, which means the surface area of the PCB winding is larger, the temperature of PCB winding is lower, and the benefit of the PCB winding is more obvious compared with the normal cable winding. According to the analysis, if the high-altitude operation, high current density, and low volume are required, PCB winding is superior to the normal cable winding.

B. Insulation at High Altitudes

Insulation at high altitudes is harsher than the sea level. The structures of the CM choke should be designed carefully to avoid the strong electrical-field (E-field) in the air gap. Paschen's law describes the relationship between the breakdown voltage, the gas pressure, and the clearance, which is depicted as (15).

$$V_B = \frac{Bpd}{\ln(Apd) + \ln\left[\ln\left(1 + \frac{1}{\gamma_{se}}\right)\right]}, \qquad (15)$$

where V_B is the breakdown voltage in volts, p is the air pressure in atms, d is the distance in meters, γ_{se} is the secondary-electron-emission coefficient and the value is 0.04498. The coefficients A and B for air are 139906 and 27737726, respectively. According to (15), the limits of E-field intensity for different clearances and air pressures are plotted in Fig. 15. According to the Fig. 15, the upper limit of E-field intensity decreases with the increasing altitude, and the E-field limit tends to a be a constant value with the increased distance. For the altitude of 50,000 ft, the E-field limit tends to be 370 V/mm. Considering some margin, 300 V/mm is set to be the upper limit of the E-field in the insulation design.

The E-field in the conventional design with the toroidal core and cable winding cannot be controlled effectively. The E-field in the gap between cables and cores are easy to exceed the limit, as shown in Fig. 16, where two AWG 2 cables are

TABLE IV
Materials of the PCB and core

Item	Material	Manufacturer	Parameters	Value
FR4	R-1766	Panasonic	Glass transition temperature	140 ℃
			Thermal decomposition temperature	315 ℃
			Dielectric constant	4.3
			Dielectric strength	20 kV/mm
Core	Hitachi FT-3M	MK Magnetics	Relative permeability @ 10 kHz	35000
			Relative permeability @ 100 kHz	15000
			Resistivity	1.2 μΩ·m
			Saturation flux density	1.23 T
			Curie temperature	570 ℃

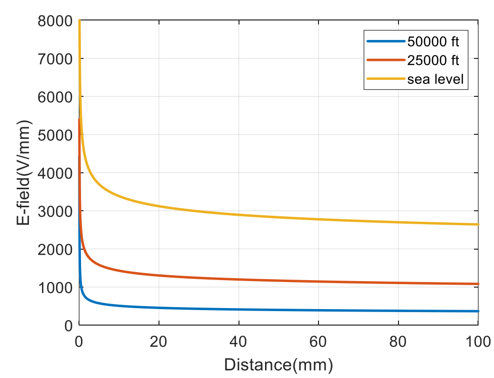

Fig. 15 The limits of E-field intensity

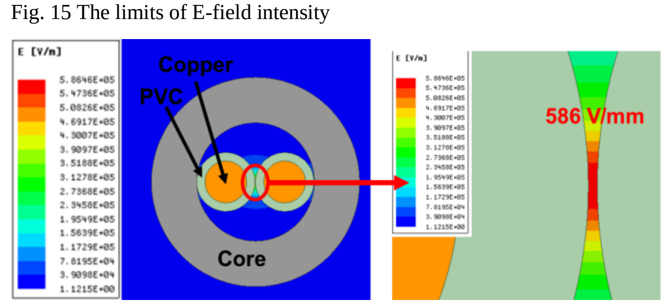

Fig. 16 The E-field distribution in the cable winding design

used. The PCB-based planar CM choke is a good option for E-field control. The cross-section of the CM choke and the E-field simulation are shown in Fig. 17. The material information of the core and PCB is shown in Table IV. Two PCB windings are placed in parallel in the window area of the core, and DC+ and DC- current flow through the two PCB windings, respectively. One PCB consists of 4 paralleled layers and the thickness of each layer is 0.5 mm. The thickness of the finished PCB is 3.5mm. The core is grounded, and the potential is defined as 0 V. The potentials of the two PCB windings are +270 V and -270 V, respectively. Some special attention is required for the E-field control in the air gaps in the choke. First, the distances h_1 and h_2 are swept to make sure the E-field between the cores and PCBs are lower than 300 V/mm. Fig. 18 (a) shows the E-field intensities between the core and the PCB with different values of h_1. Fig. 18 (b) shows E-field intensities between two PCBs with different values of h_2. Fig. 18 shows that the E-field intensity decreases as the h_1 and h_2 increases. According to the simulation results, h_1 and h_2 are set to be 3 mm and 2 mm, respectively.

To eliminate the voltage breakdown in the small gap between the edge of the PCB and the core, two grounded shielding traces are inserted on each layer of the PCB. The E-field in the air gap without the shielding traces are shown in Fig. 19. Compared with Fig. 17 (b), it can be found that with the shielding traces, the E-field in the air gap is eliminated and the air gap can be extremely small.

Another design technique for the PCB traces design is the placement of the edges of the copper traces. The distances between the copper traces and the shielding trace on external are larger than that on internal layers, as shown in Fig. 20. With such a ladder design, the E-field intensity around the corner of the copper polygons on the external layers can be reduced effectively, as shown in Fig. 20.

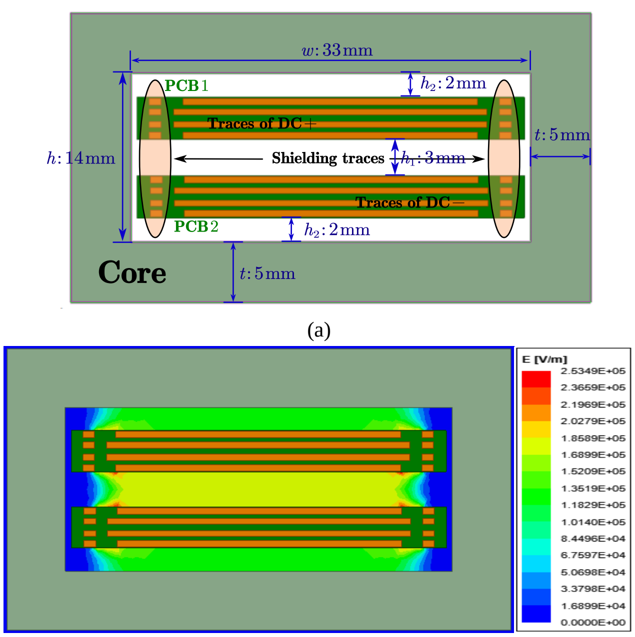

Fig. 17 The cross-section of the CM choke (a) The cross-section of the CM choke (b) The E-field simulation

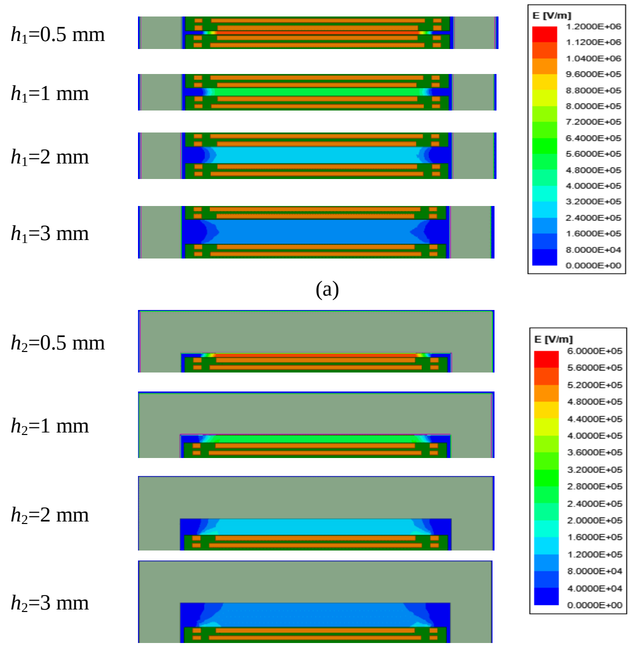

Fig. 18 The E-field intensity with different h_1 and h_2 (a) The E-field and h_1 (b) The E-field and h_2

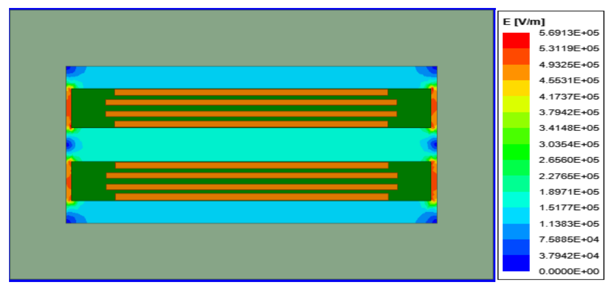

Fig. 19 The E-field simulation without shielding traces

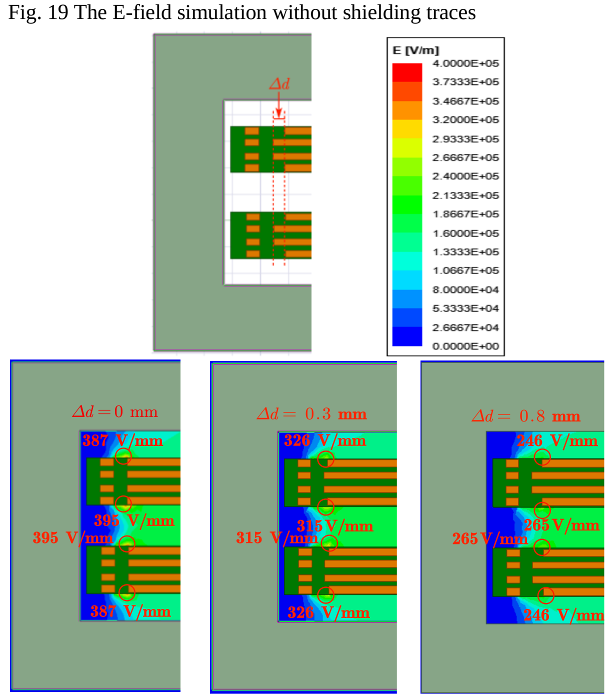

Fig. 20 The E-field simulation with different designs of the edges of copper traces

C. The Optimization of CM Choke Design

The final design of the CM choke is shown in Fig. 21. The single-turn structure is used, and two copper sheets are used to clamp the cores and the PCBs. To minimize the volume of the CM choke and meet the requirement of insulation and heat dissipation at the altitude of 50,000 ft, the dimensions of the core and the PCB windings are optimized. The flow chart of the optimization is shown in Fig. 22. The height of the window area is set to be 14 mm considering the clearance between the PCBs and core, and the maximum thickness of the PCB (3.5 mm). Another two dimensions of the core, the thickness t and the width w of the window area, are swept to find the optimal dimensions. For a specific t and w, the length l of the core can be achieved according to the required inductance (100.3 μH @ 100 kHz) and the permeability of the magnetic material.

For each round, because the natural convection coefficient and the resistivity of copper are dependent on the temperature of the PCBs, there is an iteration to determine the final temperature and power loss of the PCB windings. Finally, the low-volume map shown in Fig. 23 is obtained after all the dimensions are swept, where the PCB temperatures of all the results are below 110 ℃. The result with the lowest volume is picked and the data of the final design is shown in Table V. The influence of altitudes on the volume of the single-turn CM choke is investigated by sweeping the altitudes and obtaining the optimal design. Fig. 24 shows the minimum volume at

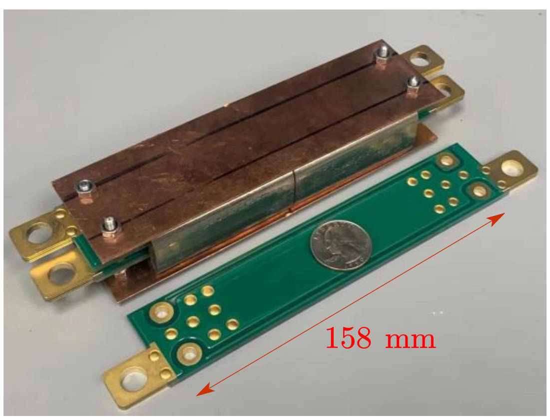

(a)

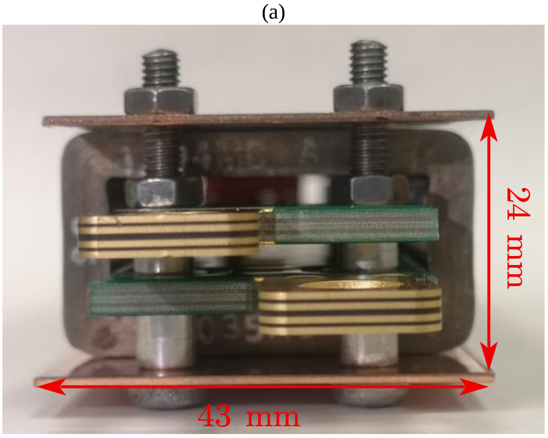

(b)

Fig. 21 The CM Choke (a) overview (b) side view

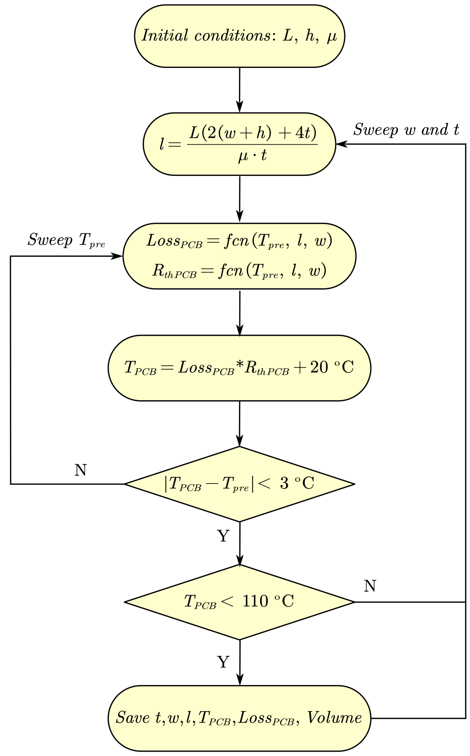

Fig. 22 The flow chart of the optimization of the choke

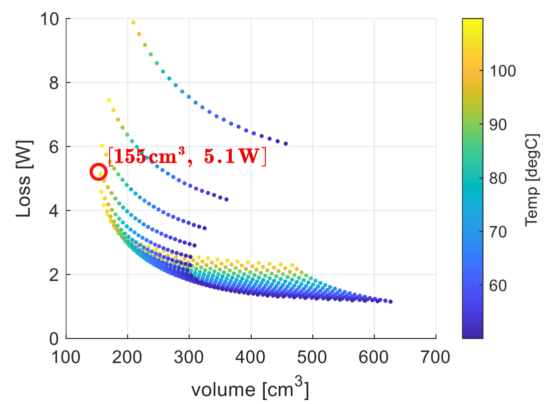

(a)

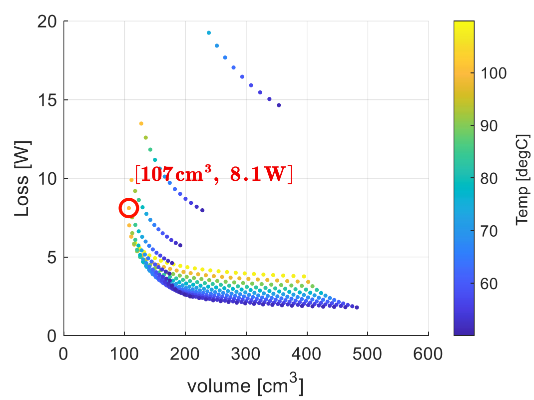

(b)

Fig. 23 The loss-volume map of the single-turn structure (a) At the altitude of 50,000 ft (b) On sea level different altitudes. The higher altitude increases the thermal resistance, and a larger surface area and core are required. Multi-turn structures are also considered for the CM choke. For multi-turn PCB windings, two layers are paralleled, and the thickness of each layer is 0.5 mm. The diagrams of each layer for two-turn and four-turn PCB windings are shown in Fig. 25. Following the same process of the single-turn structure optimization, the optimal design results with two-turn and four-turn structures are shown in Table V. The length of the core is smaller with more turns, but the width of the window area is increased because more turns mean larger total width of windings for the heat dissipation. The volume of the core is lower with the higher number of turns but the volume of the CM choke is increased, because although the volume of the cores can be reduced, a large part of the PCB winding is out of the core and takes a large space.

Table V
Data of the Multi-turns CM choke

Dimensions of the Core			
	Single turn	Two turns	Four turns
t	5 mm	3 mm	2 mm
l	121 mm	67.2 mm	41.1 mm
w	33 mm	62 mm	110 mm
h	14 mm	20 mm	18 mm
Data of the CM choke			
	Single turn	Two turns	Four turns
Inductance@100kHz	100.3 μH	100.3 μH	100.3 μH
Power loss	5.1 W	21.33 W	50.0 W
Volume	155 cm^3	422 cm^3	984.1 cm^3
PCB Temperature	108.5 °C	108.4 °C	108.7 °C

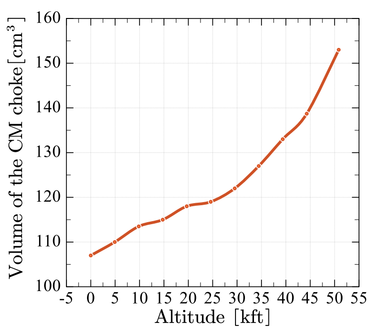

Fig. 24 The influence of altitude on the volume of single-turn CM choke

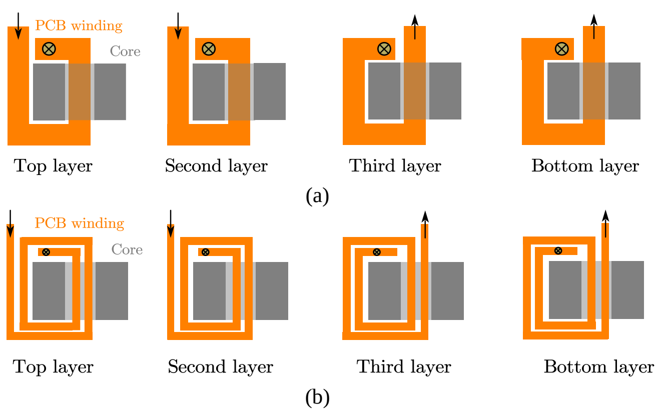

Fig. 25 Diagram of multi-turn PCB winding (a) Two-turn (b) Four-turn

IV. Experimental Results

Four experiments and tests of the CM EMI filter are conducted: CM inductance, PD, and thermal tests of the CM choke, and the CM EMI test of the 100-kW inverter/rectifier system.

First, the CM inductance of the CM choke are measured with the impedance analyzer under the air pressure of sea level and the altitude of 50,000 ft. The inductance under these two air pressures are identical and the result is shown in Fig. 26. L_{cm} at the frequency of 100 kHz is 94.3 μH, which is acceptable considering the margin left in the parameters design. For high-altitude application, some attention should be paid to avoiding air bubbles in the cores especially the bonding material. The ribbon layers are somewhat likely to delaminate under low air pressure if some air bubbles exist in the bonding material, because the air pressures in the air bubble and the external air are different at high altitudes.

The partial discharge tests are conducted in the low-pressure chamber to see the effect of air pressure on the PDIV. The diagram of the set-up is shown in Fig. 27 (a). Fig. 27 (b) shows the CM choke in the low-pressure chamber. Fig. 28 shows the PDIV at different altitudes. Three sets of tests (DC+ to ground, DC- to ground, DC+ to DC-) are done. For each set of tests, the PDIV decreases with the altitude increased, and even at the altitude of 50,000 ft, PDIV is higher than the operation voltage, which means the insulation design of the CM choke is qualified for the high-altitude operation. Take DC+ to ground test as an example, the PDIV on the sea level is up to 1786 V, but this value decreases to 603 V at the altitude of 50,000 ft, which is only about one third of the PDIV on the sea level. Fig. 29 (a)

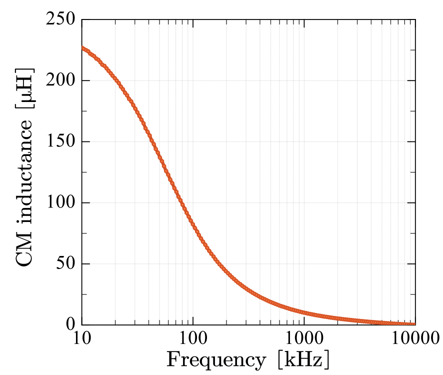

Fig. 26 The CM inductance of the CM choke

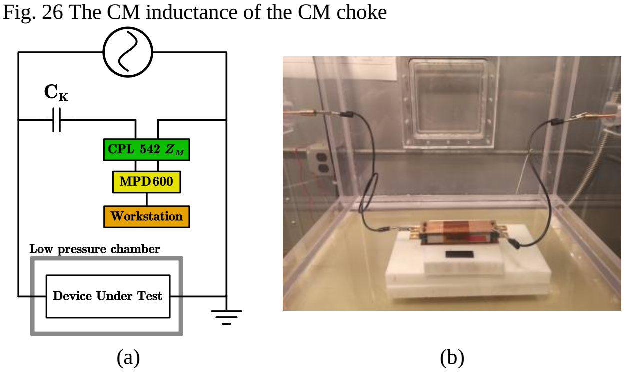

Fig. 27 The PDIV test set-up under low pressure (a) The diagram of the PDIV test set-up (b) The CM choke in the low-pressure chamber

shows the DC+ to ground PD test result on the sea level, where no PD occurs even with the excitation voltage of 1.4 kV. However, at the altitude of 50,000 ft, PD is much easier to occur. Fig. 29 (b) shows the PD test result at the altitude of 50,000 ft, where PD occurs with excitation voltage of 781.6 V. The PD occurs around the end of the shielding traces, as shown in Fig. 29(c).

The thermal tests are conducted under different air pressures. The thermal test set-up is shown in Fig. 30. The CM choke is placed in the low-pressure chamber and four thermocouples are used to obtain the temperatures of the four surfaces of the two PCBs. The temperatures of PCBs are measured without and with the cores assembled, respectively. A dc current of 190 A flows through the two PCB windings. The temperatures measured by the thermocouples and the theoretical temperatures are plotted in Fig. 31. Fig. 31 (a) shows the PCB temperatures without cores. All the PCB temperatures increase with the increasing altitudes, and the temperatures of the bottom surface of the top PCB and the top surface of the bottom PCB are a little higher than the temperatures of the other two surfaces, because the small gap between the two PCBs prevents the natural convection by some degree. The errors of PCB temperatures are within 10 ℃, except for the results without cores at the altitude of 50,000 ft. The largest error is 15 °C and happens in the temperature of upper surface of the top PCB without cores at the altitude of 50,000 ft. One possible reason is that the air flow in the low-pressure chamber is somewhat different from the real environment. Although the air pressure in the low-pressure chamber is exactly the expected value, the air flow in the chamber is not the same as the real environment because of the operation of the pump and valve. Also, according to [34], the dynamic viscosity μ and the air density ρ of air can also be affected slightly by the cooling environment, therefore, the thermal resistance can be reduced slightly, according to (13). The difference between the average temperature of the four surfaces and the theoretical temperatures is lower than 10 °C. Fig. 31(b) shows the PCB temperatures with cores assembled. Higher altitudes bring higher PCB temperature as expected. The PCB temperatures are higher than those without cores because the cores affect the ideal air convection inevitably. The errors between the theoretical temperatures and the real temperatures are lower than 10 °C.

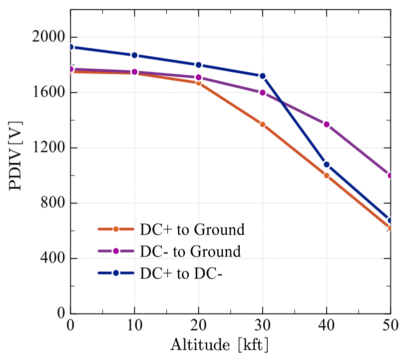

Fig. 28 The PDIV at different altitudes

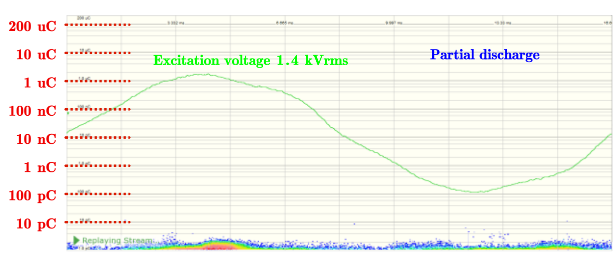

(a)

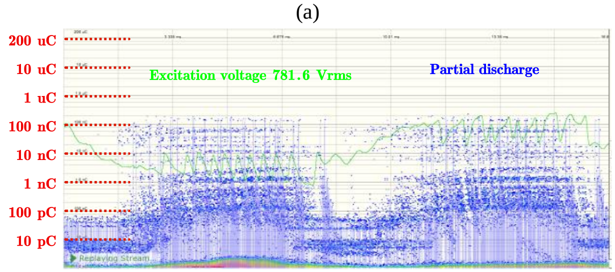

(b)

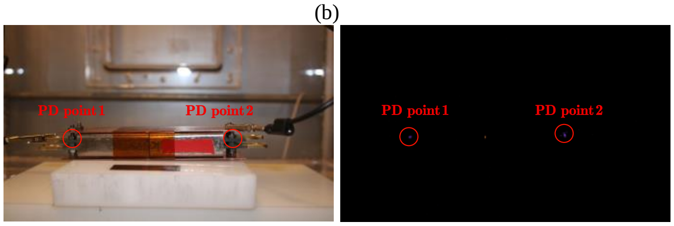

(c)

Fig. 29 The DC+ to ground PD test results with the excitation voltage of V (a) PD test result (sea level, 1.4 kV) (b) PD test result (50,000 ft, 781.6 V) (c) The PD phenomenon (50,000 ft, 781.6 V)

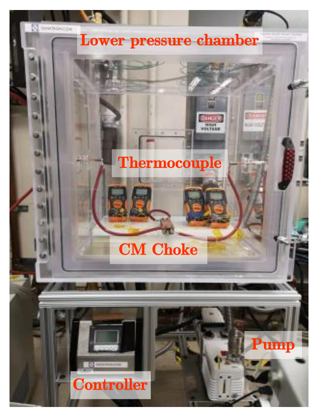

Fig. 30 The thermal test set-up

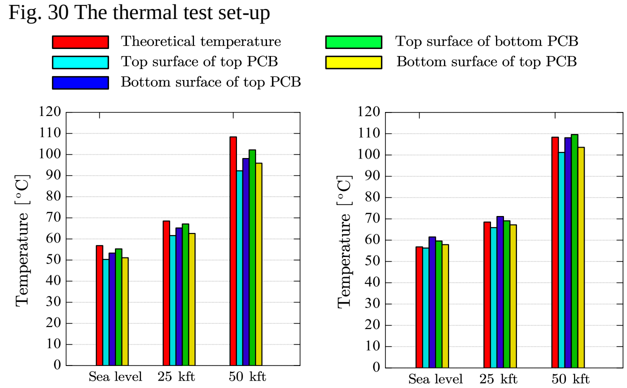

(a) (b)

Fig. 31 The temperatures obtained with thermocouples (a) without cores (b) with cores

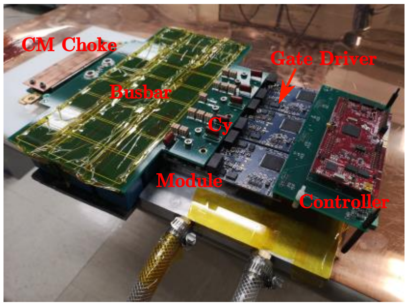

(a)

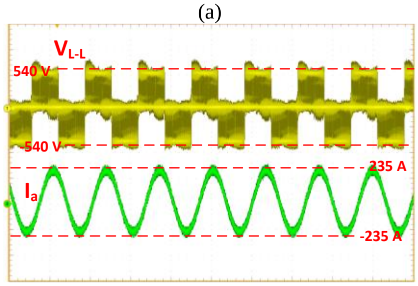

(b)

Fig. 32 The prototype and EMI test set-up of the 100-kW inverter/rectifier (a) The prototype (b) Voltage and current waveforms

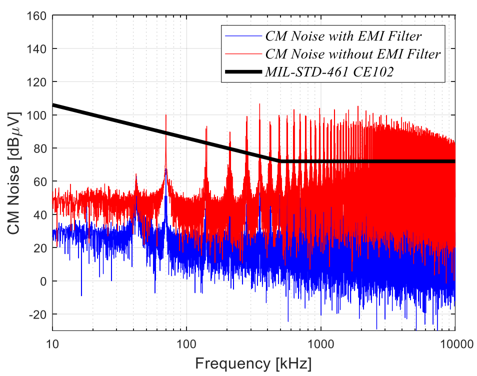

Fig. 33 The CM noise spectrum

The prototype of the 100-kW inverter/rectifier is shown in Fig. 32(a). The line-to-line voltage and phase current are shown in Fig. 32 (b). The CM noises before and after the installation of CM EMI filter are shown in Fig. 33. Fig. 33 shows that the CM EMI noise is reduced effectively with the application of the CM EMI filter, and the test result passes the EMI standard.

V. CONCLUSION

In this paper, a PCB-based planar CM EMI filter is designed for a 100-kW SiC inverter/rectifier operating at the altitude of 50,000 ft. The influence of the switching frequency on the CM inductance and the inverter/rectifier system is investigated. The required CM inductance is proportional to the switching frequency approximately. The insulation and heat dissipation at the high altitude are considered and the structure of the CM choke is optimized to achieve the minimum volume and low profile. The experimental results show that the CM noise is reduced effectively with the designed CM EMI filter. PD is eliminated at the altitude of 50,000 ft and the thermal performance is excellent with a current of 190 A.

REFERENCES

[1] B. Sarlioglu and C. T. Morris, “More Electric Aircraft: Review, Challenges, and Opportunities for Commercial Transport Aircraft,” *IEEE Transactions on Transportation Electrification*, vol. 1, no. 1, pp. 54-64, June 2015.

[2] J. Chen, Y. Shen, J. Chen, H. Bai, C. Gong and F. Wang, "Evaluation on the Autoconfigured Multipulse AC/DC Rectifiers and Their Application in More Electric Aircrafts," in *IEEE Transactions on Transportation Electrification*, vol. 6, no. 4, pp. 1721-1739, Dec. 2020,

[3] J. Liu, D. Dong and D. Zhang, "A Hybrid Modular Multilevel Converter Family With Higher Power Density and Efficiency," in IEEE Transactions on Power Electronics, vol. 36, no. 8, pp. 9001-9014, Aug. 2021.

[4] S. Yin, K. J. Tseng, R. Simanjorang, Y. Liu and J. Pou, “A 50-kW High-Frequency and High-Efficiency SiC Voltage Source Inverter for More Electric Aircraft,” *IEEE Transactions on Industrial Electronics*, vol. 64, no. 11, pp. 9124-9134, Nov. 2017.

[5] B. Cougo, H. H. Sathler, R. Riva, V. D. Santos, N. Roux and B. Sareni, "Characterization of Low-Inductance SiC Module With Integrated Capacitors for Aircraft Applications Requiring Low Losses and Low EMI Issues," in *IEEE Transactions on Power Electronics*, vol. 36, no. 7, pp. 8230-8242, July 2021.

[6] Y. Cao, M. Ngo, N. Yan, D. Dong, R. Burgos and A. Ismail, "Design and Implementation of an 18 kW 500 kHz 98.8% Efficiency High-density Battery Charger with Partial Power Processing," in IEEE Journal of Emerging and Selected Topics in Power Electronics

[7] N. Oswald, P. Anthony, N. McNeill and B. H. Stark, “An Experimental Investigation of the Tradeoff between Switching Losses and EMI Generation With Hard-Switched All-Si, Si-SiC, and All-SiC Device Combinations,” *IEEE Transactions on Power Electronics*, vol. 29, no. 5, pp. 2393-2407, May 2014.

[8] S. Zhao, X. Zhao, Y. Wei, Y. Zhao and H. A. Mantooth, "A Review on Switching Slew Rate Control for Silicon Carbide Devices using Active Gate Drivers," *in IEEE Journal of Emerging and Selected Topics in Power Electronics, doi: 10.1109/JESTPE.2020.3008344.*

[9] D. Han, C. T. Morris, W. Lee and B. Sarlioglu, "Comparison Between Output CM Chokes for SiC Drive Operating at 20- and 200-kHz Switching Frequencies," in *IEEE Transactions on Industry Applications*, vol. 53, no. 3, pp. 2178-2188, May-June 2017.

[10] Z. Fang, D. Jiang and Y. Zhang, "Study of the characteristics and suppression of EMI of inverter with SiC and Si devices," in *Chinese Journal of Electrical Engineering*, vol. 4, no. 3, pp. 37-46, September 2018, doi: 10.23919/CJEE.2018.8471288.

[11] Henry Wong, Robert E. Peck, “Experimental Evaluation of Air-Cooling Electronics at High Altitudes,” *Journal of Electronic Packaging*, vol. 123, pp. 356, 2001.

[12] C. L. Belady, “Design considerations for air cooling electronic systems in high altitude conditions,” *IEEE Transactions on Components, Packaging, and Manufacturing Technology: Part A*, vol. 19, no. 4, pp. 495-500, Dec. 1996.

[13] *IEEE Standard for Switchgear Assemblies Including Metal-Enclosed Bus.* IEEE STD.27, 1974.

[14] D. A. Hall, “Prediction of electronic component temperatures at high altitude using low altitude measurements,” *Fifth Annual IEEE Semiconductor Thermal and Temperature Measurement Symposium*, San Diego, CA, USA, 1989, pp. 121-125.

[15] G. E. Heberlein, C. Malkowski and M. J. Cibulka, “The effect of altitude on the operation performance of low-voltage switchgear and controlgear components,” *IEEE Transactions on Industry Applications*, vol. 38, no. 1, pp. 189-194, Jan.-Feb. 2002.

[16] Doron Bar-Shalom. “Altitude effects on heat transfer processes in aircraft electronic equipment cooling”. Massachusetts Institute of Technology. 1989

[17] Xu, Guoping. “Thermal Performance Prediction for High Power Processors at High Altitude,” *Proceedings of the ASME 2005 International Mechanical Engineering Congress and Exposition. Electronic and Photonic Packaging, Electrical Systems*

Design and Photonics, and Nanotechnology. Orlando, Florida, USA. November 5–11, 2005. pp. 549-554. ASME.

[18] Evan M. Racine. “Experimental study - high altitude forced convective cooling of electromechanical actuation systems”. University of Dayton. 2015.

[19] H. Wong, “Experimental Investigation of Air Cooling Electronics at High Altitudes”. Arizona State University, 1999.

[20] J. Xue and F. Wang, “A practical liquid-cooling design method for magnetic components of EMI filter in high power motor drives,” 2016 IEEE Energy Conversion Congress and Exposition (ECCE), Milwaukee, WI, 2016, pp. 1-6.

[21] Y. Liu et al., "LCL Filter Design of a 50-kW 60-kHz SiC Inverter with Size and Thermal Considerations for Aerospace Applications," in IEEE Transactions on Industrial Electronics, vol. 64, no. 10, pp. 8321-8333, Oct. 2017, doi: 10.1109/TIE.2017.2677338.

[22] E. Husain and R. S. Nema, “Analysis of Paschen Curves for air, N2 and SF6 Using the Townsend Breakdown Equation,” *IEEE Transactions on Electrical Insulation*, vol. EI-17, no. 4, pp. 350-353, Aug. 1982.

[23] Z. Yuan et al., "Insulation and Switching Performance Optimization for Partial-discharge Free Laminated Bus Bar In More-electric Aircraft Applications," in IEEE Transactions on Power Electronics,

[24] J. Hu, X. Zhao, L. Ravi, R. Burgos, and D. Dong, "Enhanced Gate Driver Design for SiC-Based Generator Rectifier Unit for Airborne Applications," 2021 IEEE Applied Power Electronics Conference and Exposition (APEC), 2021.

[25] Y. Wang, T. Balachandran, Y. Hoole, Y. Yin and K. S. Haran, “Partial Discharge Investigation of Form-Wound Electric Machine Winding for Electric Aircraft Propulsion,” *IEEE Transactions on Transportation Electrification*, vol. 6, no. 4, pp. 1638-1647, Dec. 2020.

[26] Y. Wang *et al*., “Partial Discharge Investigation of Form-Wound Electric Machine Winding for Electric Aircraft Propulsion,” *IEEE Transactions on Transportation Electrification*, vol. 7, no. 1, pp. 78-90, March 2021.

[27] D. Rothmund, T. Guillod, D. Bortis and J. W. Kolar, “99% Efficient 10 kV SiC-Based 7 kV/400 V DC Transformer for Future Data Centers,” *IEEE Journal of Emerging and Selected Topics in Power Electronics*, vol. 7, no. 2, pp. 753-767, June 2019.

[28] H. Song, J. Wang, Y. Xu, R. Burgos and D. Boroyevich, “A High-Density Single-Turn Inductor for a 6 kV SiC-based Power Electronics Building Block,” *2020 IEEE Applied Power Electronics Conference and Exposition (APEC)*, 2020, pp. 1127-1134.

[29] A. Binder and A. Muetze, "Scaling Effects of Inverter-Induced Bearing Currents in AC Machines," in IEEE Transactions on Industry Applications, vol. 44, no. 3, pp. 769-776, May-june 2008.

[30] Y. Huang et al., "Analytical Characterization of CM and DM Performance of Three-Phase Voltage-Source Inverters Under Various PWM Patterns," in IEEE Transactions on Power Electronics, vol. 36, no. 4, pp. 4091-4104, April 2021.

[31] O. Ojo, “The generalized discontinuous PWM scheme for three-phase voltage source inverters,” *IEEE Transactions on Industrial Electronics*, vol. 51, no. 6, pp. 1280-1289, Dec. 2004.

[32] Z. Zhao, F. Diao, Y. Wu, Z. Wang and Y. Zhao, "DC-Link Capacitor Current Modeling and Analysis for Three-Level Voltage Source Inverters," 2021 IEEE Applied Power Electronics Conference and Exposition (APEC), 2021, pp. 2434-2439

[33] R. Lai et al., "A Systematic Topology Evaluation Methodology for High-Density Three-Phase PWM AC-AC Converters," in IEEE Transactions on Power Electronics, vol. 23, no. 6, pp. 2665-2680, Nov. 2008

[34] [Jack_P._Holman] “Heat_Transfer”. Tenth_Edition